research papers

Ultrahigh-resolution study on *Pyrococcus abyssi* rubredoxin. I. 0.69 Å X-ray structure of mutant W4L/R5S

Heiko Bönisch,[a]* Christian L. Schmidt,[b] Pierre Bianco[c] and Rudolf Ladenstein[a]

[a]Karolinska Institutet, Department of Biosciences at NOVUM, Center for Structural Biochemistry, Hälsovägen 7-9, S-14157 Huddinge, Sweden, [b]Department of Biochemistry, University of Lübeck, Ratzeburger Allee 160, D-23538 Lübeck, Germany, and [c]BIP/CNRS, 31 Chemin Joseph-Aiguier, 13402 Marseille CEDEX 20, France

Correspondence e-mail:
heiko.bonisch@csb.ki.se

The crystal structure of *Pyrococcus abyssi* rubredoxin mutant W4L/R5S was solved by direct methods. The model of the air-oxidized protein was refined by partially restrained full-matrix least-squares refinement against intensity data to 0.69 Å resolution. This first ultrahigh-resolution structure of a rubredoxin provides very detailed and precise information about the $Fe(SCys)_4$ centre and its environment, the peptide-backbone stereochemistry, H atoms and hydrogen bonds, static and dynamic disorder, the solvent structure and the electron-density distribution. *P. abyssi* rubredoxin W4L/R5S is the first of a series of mutants studied by atomic and ultrahigh-resolution X-ray crystallography which are expected to contribute to the understanding of structure–function relationships in iron–sulfur proteins.

1. Introduction

Rubredoxins (Rds) occur in several mostly anaerobic bacteria and archaea and are small redox proteins of typically 52–54 amino-acid residues with a single $Fe(SCys)_4$ centre. They are involved in electron-transfer reactions in superoxide, nitrate and sulfur reduction (Jenney *et al.*, 1999). Owing to their small size, the availability of high-resolution structures and the large amount of accumulated data, rubredoxins have been used as model systems in a large number of experimental and theoretical studies, for example on protein thermostability, protein folding, electron-transfer mechanisms and structural determinants of the redox potential.

Pyrococcus abyssi (Pa) is an obligate heterotrophic and anaerobic hyperthermophilic archaeon that was isolated from a deep-sea hydrothermal vent. It has an optimum growth temperature of at least 372 K under 20 MPa pressure, grows by fermentation of peptides or amino acids and is able to reduce elemental sulfur (Erauso *et al.*, 1993). The sequencing of the Pa genome (Cohen *et al.*, 2003) provided the opportunity to use PaRd in a study combining site-directed mutagenesis, spectroscopy and high-resolution X-ray crystal-lography. The original motivation was to use PaRd as a small model system to investigate structural determinants of the redox potential and the spectroscopic properties of Rieske iron–sulfur proteins, which show similarities in the structure of their metal-binding site to that of Rd (Iwata *et al.*, 1996). Based on knowledge of the structural dependence of the redox potential in Rieske proteins, several mutants were designed and overproduced in *Escherichia coli*. The wild-type enzyme (WT) and those mutants which turned out to be stable

and redox-active were characterized by spectroscopy and cyclic voltammetry and structure solution by X-ray crystallography was attempted. The W4L/R5S mutant was not designed by intention; it is a modification of a W4L/R5C mutant that occurred during gene amplification by PCR and that was accidentally selected owing to the high expression level. Crystallization experiments with the W4L/R5S mutant produced unusually well diffracting crystals and provided the unique opportunity to perform an ultrahigh-resolution study on PaRd.

To date (January 2005), 37 X-ray and neutron diffraction structures of five different Rds have been deposited in the Protein Data Bank (Berman *et al.*, 2000). Nine of these structures have been refined to atomic resolution, *i.e.* to a resolution of at least 1.2 Å as defined by Sheldrick (1990), with the highest resolutions of 0.95 and 0.92 Å reported for Rds from *P. furiosus* (PfRd; Bau *et al.*, 1998) and *Desulfovibrio vulgaris* (DvRd; Z. Dauter, S. Butterworth, L. C. Sieker, G. Sheldrick & K. S. Wilson, unpublished work; PDB code 1rb9), respectively. For *D. gigas* Rd (DgRd) data collection and structure determination at 0.68 Å resolution have been reported (Chen *et al.*, 2003), but no refined structure has yet been published. The advantages of macromolecular crystallography at atomic resolution have been discussed in several reviews (Dauter *et al.*, 1997; Schmidt & Lamzin, 2002; Esposito *et al.*, 2002). The high level of detail visible in the electron-density maps and the precise determination of atomic positions with low coordinate error allow a detailed and reliable structural analysis and the application of complementary methods such as quantum-chemical calculations and molecular modelling. An additional level of information becomes available at subatomic or ultrahigh resolution below 0.8 Å, as details of the electron-density distribution now become visible (Jelsch *et al.*, 2000). The assumption of spherical atoms no longer holds, as the deformation of the electron density by covalent bonds and electrostatic interactions is observable and has to be accounted for. Analysis of the electron-density distribution at ultrahigh resolution allows the direct determination of bond orders and charge distributions in the structure. The number of ultrahigh-resolution protein structures is still limited; to date (January 2005), eight protein structures with a resolution equal to or better than 0.8 Å have been deposited in the PDB: crambin (0.54 Å; Jelsch *et al.*, 2000), antifreeze protein Rd1 (0.62 Å; Ko *et al.*, 2003), human aldose reductase (0.66 Å; Howard *et al.*, 2004), syntenin Pdz2 (0.73 Å; Kang *et al.*, 2004), *Bacillus lentus* subtilisin (0.78 Å; Kuhn *et al.*, 1998), *Thermochromatium tepidum* HiPIP (0.80 Å; Liu *et al.*, 2002), trypsin (0.80 Å; Schmidt *et al.*, 2003) and carbohydrate-binding domain Cbm36 (0.80 Å; Jamal *et al.*, 2004).

Here, we present the 1.79 Å structure of the PaRd wild-type protein and the structure of mutant W4L/R5S refined to 0.69 Å resolution, the first ultrahigh-resolution structure of a rubredoxin. In the following, we will describe some of the information available from analysis of the PaRd W4L/R5S structure and discuss the relevance of ultrahigh-resolution data for the investigation of the structure and function of iron–sulfur proteins.

2. Materials and methods

2.1. Construction of the expression clones and mutagenesis

A gene encoding the rubredoxin from *P. abyssi* (GenBank accession No. CAB49806) with a codon usage optimized for *E. coli*, including an *Nco*I site at the 5′-end and a *Bam*HI site at the 3′-end, was synthesized from four oligonucleotides (Paby_Nt1, TACCGTCCATGGCGAAATGGCGTTGCAA-AATTT; Paby_Nt2, GGCGTTGCAAAATTTGTGGCTA-TATCTATGATGAAGATGAAGGTGATCCGGATAACG-GTATCAGCCCGGGTACCAAATTTGAA; Paby_Ct1, GC-GTTCAAATTCGCTTTTCGGCGCGCCACACAGCGGA-CACACCCAGTCATCCGGCAGATCTTCAAATTTGGT-ACCCGGGC; Paby_Ct2, AGTGGATCCTTATTCAATGC-GTTCAAATTCGCTT) using PCR methods. The PCR product was purified by chloroform–phenol extraction, digested with *Bam*HI and *Nco*I and purified by agarose gel electrophoresis. The purified insert was ligated into an accordingly prepared pet15b (Novagen) vector. The ligated plasmids were transformed into *E. coli* BL21-Gold (DE3) cells (Stratagene). Six colonies were tested for the expression of the rubredoxin as described by Schmidt *et al.* (1997). Four of the clones expressed a rubredoxin-like protein as judged by SDS–PAGE and UV–Vis spectroscopy (data not shown). One of these clones showed a significant higher level of expression. DNA sequencing revealed the presence of two point mutations, resulting in the production of a mutant protein with the amino-acid exchanges W4L and R5C. To prevent possible complications owing to the presence of a fifth potential ligand for the iron ion, a standard PCR mutagenesis procedure using the primers Rr_nm (ATTTGTGGCTATATCTATGATGAA GATGAA) and Rr_C5S (TTTGCAACTCAATTTCGC-CATGGTATA) was used to construct a gene encoding the W4L/R5S mutant of the protein, which retained the high level of expression (data not shown).

2.2. Large-scale expression and purification of the rubredoxins

Large-scale expression of the rubredoxins was performed essentially as described by Schmidt *et al.* (1997) with two slight modifications: the addition of cysteine to the induction medium was omitted and the optimal iron concentration in the induction medium was determined to be 0.3 m*M* (data not shown). All purification steps were performed at 273–277 K.

The *E. coli* cell pellet was resuspended in 50 m*M* Tris–HCl pH 7.5, 1 m*M* EDTA and broken by sonication. The suspension was centrifuged for 20 min at 18 000 rev min⁻¹ in a Sorvall SS34 rotor to remove cell debris. The membranes were removed by a second centrifugation for 60 min at 38 000 rev min⁻¹ in a Contron TFT45 rotor. MgSO$_4$ to a final concentration of 7 m*M* and 1000 units of benzonase (Merck, Darmstadt, Germany) were added to 45 ml of the supernatant (equivalent to the cells from 3 l medium). The solution was incubated for 90 min at 310 K and subsequently centrifuged for 30 min at 4000*g*. The clear supernatant was concentrated to a final volume of 7 ml on a membrane with a 3 kDa cutoff, centrifuged for 10 min at 10 000*g* and loaded at a flow rate of

Table 1
Data-collection statistics.

Values in parentheses are for the last resolution shell.

Data set	WT	W4L/R5S†
No. of crystals	1	1
Crystal dimensions (mm)	$0.3 \times 0.3 \times 0.3$	$0.4 \times 0.4 \times 0.4$
Temperature (K)	286	100
Resolution range (Å)	40.37–1.79 (1.81–1.79)	20.00–0.69 (0.70–0.69)
Space group	$P2_12_12_1$	$P2_12_12_1$
Unit-cell parameters (Å)	$a = 54.30$, $b = 59.51$, $c = 80.74$	$a = 25.14$, $b = 39.50$, $c = 45.07$
No. of observations	361281	532171
No. of observed unique reflections	24841	70714
Completeness (%)	98.1 (89.0)	94.5 (90.4)
Average redundancy	14.3	7.1
Mosaicity (°)	0.6	0.3
$\langle I/\sigma(I) \rangle$	11.7 (2.5)	13.7 (1.6)
R_{sym} (%)	9.0 (50.4)	3.9 (22.0)
Wilson B factor (Å^2)	21.9	3.6

† Statistics for merged Friedel pairs.

1 ml min^{-1} onto a Sephacryl S100 HR (Amersham Pharmacia) column (2.6 cm diameter, 100 cm length) equilibrated and eluted with 25 mM Tris–HCl pH 7.5, 0.2 mM EDTA and 100 mM NaCl. The rubredoxin-containing fractions (judged by colour and SDS–PAGE) were pooled, concentrated to a volume of 15 ml and centrifuged as above. 5 ml of the supernatant was loaded at 1 ml min^{-1} onto a HiLoad 16/60 Superdex 30 prep-grade (Amersham Pharmacia) column equilibrated and eluted with 25 mM Tris–HCl pH 7.5, 0.2 mM EDTA and 50 mM NaCl. Fractions containing pure rubredoxin (judged by SDS–PAGE) were concentrated as above and desalted by repeated dilution with 25 mM Tris–HCl pH 7.5 and subsequent concentration.

The holo and apo forms of the rubredoxins were separated by ion-exchange chromatography on a Poros 20 HQ 4.6/100 column (Applied Biosystems). The column was equilibrated with 20 mM MES–NaOH pH 6.0 and eluted with a gradient from 0 to 400 mM NaCl in 70 ml buffer at a flow rate of 2 ml min^{-1}. The fractions containing the pure holoprotein as judged by UV–Vis spectroscopy were combined, concentrated and desalted as above and stored at 253 K.

2.3. Electrochemical techniques

Redox-potential values were obtained from cyclic and square-wave voltammetry experiments carried out using an EG&G 6310 Electrochemical Impedance Analyzer modulated by EG&G *PAR M* 270/250 software. Square-wave voltammograms were performed using 5 Hz as the square-wave frequency and 2 mV as the pulse-height amplitude. A conventional three-electrode system consisting of a Metrohm Ag/AgCl/NaCl$_{(sat)}$ reference electrode, a gold-wire auxiliary and a pyrolytic graphite electrode as the working electrode was used throughout. Because of the low isoelectric points of the proteins, virtually no responses were observed in the absence of a promoter. For this reason, all experiments were performed in the presence of polycationic poly-L-lysine (18 µM) in order to increase the electron-transfer rate.

Potentials *versus* the standard hydrogen electrode were converted by adding 210 mV to the measured values.

2.4. Protein crystallization

Protein crystals of PaRd WT were grown in 2.6 M ammonium sulfate, 0.1 M MES pH 5.8 and 3%(v/v) dioxane using the sitting-drop vapour-diffusion method at 293 K. The concentration of the protein stock solution was 33 mg ml^{-1} in 25 mM Tris–HCl pH 7.5. Addition of dioxane was necessary to avoid the formation of crystal clusters owing to excessive nucleation.

Crystals of PaRd W4L/R5S for data collection under cryogenic conditions were grown in 3.0–3.4 M sodium malonate pH 6.0 using the sitting-drop vapour-diffusion method at 293 K and a protein stock solution of 27.6 mg ml^{-1} in 25 mM Tris–HCl pH 7.5. Crystals became visible after approximately 12 h and reached their final size of 1–2 mm maximum length after 1–2 weeks.

2.5. Data collection

A single crystal of PaRd WT was used to collect a complete data set to 1.79 Å resolution at room temperature (286 K). The crystal was mounted in a capillary and X-ray diffraction data were collected at a wavelength of 1.5418 Å using a Siemens rotating-anode X-ray generator operated at 45 kV and 100 mA (Cu $K\alpha$ radiation, graphite monochromator, 0.3 mm collimator) and a 30 cm MAR image-plate detector (MAR Research, Germany). 180 rotation images were collected with a rotation angle of 1° and an exposure time of 300 s. With a single crystal of PaRd W4L/R5S grown in 3.4 M sodium malonate pH 6.0, ultrahigh-resolution data were collected at EMBL beamline BW7A (DESY, Hamburg, Germany) equipped with a MAR CCD detector. Sodium malonate worked as an effective cryoprotectant and the crystal could be mounted directly for data collection at 100 K. Using a wavelength of 0.7301 Å and the minimal possible crystal-to-detector-distance of 35 mm, a complete data set to 0.69 Å resolution was collected, consisting of 160 rotation images with a rotation angle of 0.5°. Low-resolution reflections which saturated the CCD detector were collected in a second data set of 90 rotation images to 1.42 Å resolution (rotation angle 1.0°).

The raw data were processed with *DENZO* and *SCALE-PACK* (Otwinowski & Minor, 1997). For the two data sets of PaRd W4L/R5S Friedel pairs were kept separate in the output file using the ANOMALOUS flag. Data-collection statistics are given in Table 1.

2.6. Structure solution and refinement

The structure of PaRd WT was solved by molecular replacement with *AMoRe* (Navaza, 1994) using the 0.95 Å structure of PfRd (Bau *et al.*, 1998) as a search model. Four Rd molecules were located in the asymmetric unit (AU). The model was refined by restrained maximum-likelihood refinement with *REFMAC* (Murshudov *et al.*, 1997) with individual isotropic temperature factors. Solvent was modelled using

Table 2
Refinement statistics and stereochemistry of the final model.

	W4L/R5S	WT
Resolution range (Å)	20.00–0.69	40.37–1.79
Residue range	2–53	1–53
No. of non-H protein atoms	471 (132)†	1841
No. of H atoms	448 (158)†	0
No. of water sites	94 (22)†	157
R_{work} (%) (working set, all reflections)	10.03 (126138)‡	15.8 (23573)‡
R_{work} (%) [working set, $F_{\mathrm{o}} > 4\sigma(F_{\mathrm{o}})$]	8.74 (94176)‡	
R_1 (%) (working + test set, all reflections)	10.01 (132784)‡	
R_1 (%) [working + test set, $F_{\mathrm{o}} > 4\sigma(F_{\mathrm{o}})$]	8.72 (99101)‡	
R_{free} (%) (test set, all reflections)	10.83 (6646)‡	19.1 (1266)‡
R_{free} (%) [test set, $F_{\mathrm{o}} > 4\sigma(F_{\mathrm{o}})$]	9.47 (4925)‡	
No. of parameters	5141	
No. of observations/No. of parameters	25.8	
No. of restraints	1619	
Mean isotropic B factor (Å^2)		
All atoms	8.9	26.7
Main-chain atoms	4.8	23.3
Side-chain atoms	9.0	29.5
Solvent	18.5	41.7
Mean anisotropy (A)§		
Protein atoms	0.449 (0.183)	
Heteroatoms	0.611	
Solvent	0.275 (0.143)	
Total	0.420 (0.189)	
R.m.s. deviations from ideal geometry (for fully restrained refinement)		
Bond length (1–2) (Å)	0.026	0.019
Angle distance (1–3) (Å)	0.057	
Bond angle (°)		1.712
Zero chiral volume (Å^3)	0.115	
Non-zero chiral volume (Å^3)	0.125	0.122
Deviations from planes (Å)	0.043	0.008
Ramachandran plot¶		
Residues in most favored regions (%)	95.0	96.3
Residues in additionally allowed regions (%)	5.0	3.7

† The number of atoms with partial occupancy is given in parentheses. ‡ The number of reflections is given in parentheses. § Calculated using *PARVATI* (Merritt, 1999). $\sigma(A)$ is given in parentheses. ¶ Calculated using *PROCHECK* (Laskowski *et al.*, 1993).

alternating cycles of *REFMAC* and *ARP* (Lamzin & Wilson, 1997). The solvent model was inspected after each round and solvent molecules with B factors higher than 60 Å^2 and density below 1σ in a $2mF_{\mathrm{o}} - DF_{\mathrm{c}}$ difference map were removed. Model building was performed in *O* (Jones *et al.*, 1991). Refinement statistics are given in Table 2.

The structure of PaRd W4L/R5S was solved by direct methods employing *SHELXD* (Sheldrick, 1998). The atomic positions output by *SHELXD* were identified by comparison with a molecular-replacement solution for PaRd W4L/R5S refined to 1.64 Å resolution (results not shown). An isotropic temperature factor of 3 Å^2 was assigned to all atoms, corresponding to the Wilson B factor.

The refinement of the model was performed with *SHELXL* (Sheldrick & Schneider, 1997). Each round of refinement consisted of ten cycles of conjugate-gradient least-squares refinement against the intensities of 132 784 reflections. The Friedel pairs were treated as independent reflections. For Fe and S atoms, corrections for anomalous dispersion (f', f'') were input for a wavelength of 0.73 Å. 6646 reflections (5%) were randomly chosen as reference set for cross-validation

analysis (Brünger, 1992). The geometry of the model was not restrained; standard geometrical restraints were introduced only for disordered atoms during the refinement. No anti-bumping restraints were used for protein and solvent. A diffuse solvent model (Tronrud, 1997) was used throughout. Water molecules automatically introduced by *SHELXL* were analyzed manually after each round of refinement. The occupancy of solvent molecules was not refined and the occupancy of partially occupied solvent sites was set to 0.5. Model building was performed within *O* (Jones *et al.*, 1991).

After a first round of refinement of the initial model from *SHELXD* ($R_{\mathrm{free}} = 23.98\%$), most of the missing main-chain and side-chain atoms could be modelled. Water molecules were included into the model and the disorder of main-chain and side-chain atoms was modelled ($R_{\mathrm{free}} = 17.46\%$). Anisotropic atomic displacement parameters for all non-H atoms were introduced, resulting in a significant decrease of R_{free} by 3.4% ($R_{\mathrm{free}} = 14.07\%$). Anisotropic atomic displacement parameters in the direction of covalent bonds were restrained by a rigid-bond restraint. Riding H atoms were added to the model and refined with isotropic temperature factors set by default to 1.2 or 1.5 times the B factor of the bound atom ($R_{\mathrm{free}} = 11.81\%$). The orientation of $-\mathrm{NH}_3^+$, $-\mathrm{CH}_3$ and $-\mathrm{OH}$ groups was refined if the protons were observable (*SHELXL* commands HFIX 137 and HFIX 147). After modelling of solvent disorder, a final round of conjugate-gradient least-squares refinement consisting of 20 cycles with adjusted weight was performed ($R_{\mathrm{free}} = 10.85\%$). Thereafter, the refinement procedure was changed to full-matrix least-squares refinement using *SHELXH*. Owing to the small size of the molecule it was not necessary to block the refinement, but the damping factors had to be increased in order to keep the refinement stable ($R_{\mathrm{free}} = 10.83\%$). In the final round the model was refined against all intensities. For the calculation of estimated standard uncertainties one cycle of full-matrix least-squares refinement was performed without restraints, damping and application of shifts. The refinement statistics are given in Table 2.

3. Results and discussion

3.1. Protein crystallization and crystal packing

The protein crystallization of PaRd WT and W4L/R5S represents a good example for the potential influence of point mutations on the crystallization behaviour of biological macromolecules. PaRd WT crystallized from ammonium sulfate, sodium malonate or sodium/potassium phosphate as clusters of very small crystal plates. Seeding techniques (streak-seeding or macroseeding) and additives (dioxane, *n*-propanol or PEG 400) had to be used in order to obtain single crystals suitable for X-ray diffraction experiments. However, these crystals did not diffract to atomic or ultrahigh resolution. The crystal used for data collection belonged to the orthorhombic space group $P2_12_12_1$, with unit-cell parameters $a = 54.30$, $b = 59.51$, $c = 80.74$ Å, and contained four Rd molecules in the AU.

PaRd W4L/R5S showed a significantly different crystallization behaviour. Using ammonium sulfate or sodium malonate as precipitant, large single crystals diffracting to ultrahigh resolution were obtained routinely within one to two weeks without additives or seeding. These crystals also belonged to space group $P2_12_12_1$, but with a smaller unit cell ($a = 25.14$, $b = 39.50$, $c = 45.07$ Å) and only one Rd molecule in the AU, reflecting significant differences in crystal packing (Fig. 1). The Rd molecules in the WT crystal showed an unusually low crystal packing density for such a small molecule, with a solvent content of 55% (Matthews coefficient $V_M = 2.77$ Å^3 Da^{-1}). This high solvent content is correlated with the presence of two large parallel solvent channels in the crystal. In contrast, the molecules in the PaRd W4L/R5S
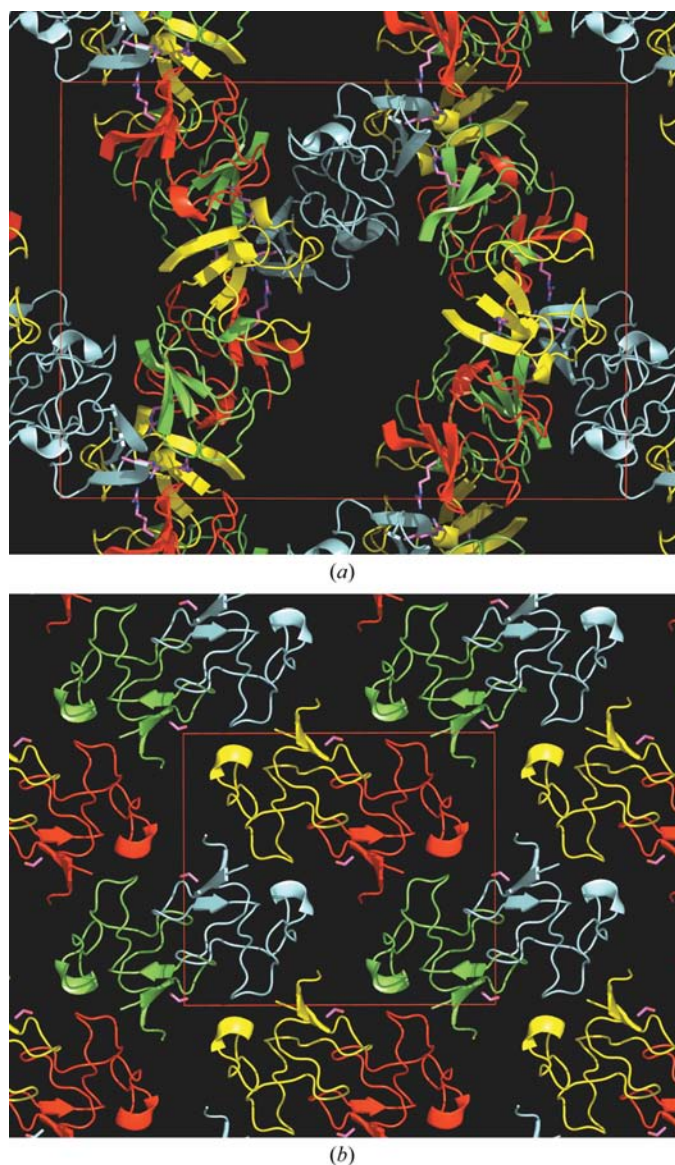
crystal were tightly packed with a low solvent content of 27% (Matthews coefficient $V_M = 1.69$), which is at the lower end of the solvent-content range reported for crystals diffracting to atomic or subatomic resolution (Schmidt & Lamzin, 2002). This change in crystal packing was most likely triggered by the R5S point mutation. Whereas the W4L mutation exchanged two residues in the hydrophobic core of the molecule, the R5S mutation replaced a solvent-exposed arginine residue by serine (Fig. 4). The analysis of crystal contacts showed that Arg5 was part of a small network of hydrogen bonds and salt bridges that formed the main interaction between neighbouring molecules in the PaRd WT crystal. Thus, it is plausible to conclude that the replacement of this arginine residue caused the change in crystal packing. In PfRd (Bau et al., 1998) and DgRd (Chen et al., 2003), for which data collection to sub-ångström resolution was reported, a valine or threonine residue is present at this position. The exchange of charged flexible side chains with high conformational entropy such as lysine and arginine has been used intentionally in some structure-based efforts to improve the packing and diffraction qualities of protein crystals (Longenecker et al., 2001; Mateja et al., 2002). In the PaRd W4L/R5S crystal, the Rd molecule in the AU formed a total of 12 direct hydrogen bonds and four salt bridges to six neighbouring molecules, compared with an average of six direct hydrogen bonds (five hydrogen bonds involving Arg5) and two salt bridges for each of the four molecules in the AU of the PaRd WT crystal. This larger number of strong crystal contacts was very likely to be responsible for the significant improvement in resolution by reducing the disorder of the PaRd W4L/R5S molecules in the crystal, which was reflected by the large difference in the overall B factor (Table 1). A disadvantage of the changed crystal packing in the PaRd W4L/R5S crystal was a slight distortion of the first metal-binding turn by crystal contacts (see below). Site-directed mutagenesis experiments are in progress to address this problem.

3.2. Structure solution and refinement

The availability of ultrahigh-resolution data for PaRd W4L/R5S offered the possibility of obtaining an unbiased starting model by application of direct methods (Chen et al., 2003; Mukherjee, 1999; Sheldrick et al., 1993). The structure solution by *SHELXD* was fast (approximately 3.5 h; 2 × Intel Xeon 2.8 GHz, 2 GB RAM) and straightforward, and provided a model of high quality.

Compared with a molecular-replacement solution for PaRd W4L/R5S refined to 1.64 Å resolution (results not shown), 357 of 403 non-H protein atoms (89%) were placed correctly with an r.m.s. displacement of 0.271 Å. The model could be used directly as a starting model for refinement in *SHELXL*.

The refinement in *SHELXL* followed the general strategy for the refinement of macromolecular structures at atomic resolution as outlined by Sheldrick & Schneider (1997), but with two exceptions. In order to avoid potential bias of the PaRd W4L/R5S structure towards idealized restraint target values, an attempt was made to refine the model without

Figure 1
Packing of *P. abyssi* rubredoxin molecules in the protein crystal. (*a*) Wild type, (*b*) mutant W4L/R5S. The four molecules in the asymmetric unit of the wild-type protein and the four molecules in the unit cell of mutant W4L/R5S are coloured cyan, red, yellow and green. The side chain of residue Arg5/Ser5 is shown in magenta.

geometrical restraints. For the same reason no antibumping restraints were used for the protein and the solvent. Because of the very high quality of the electron-density map, most of the atomic positions in PaRd W4L/R5S were exactly defined and could be refined without restraints. For 15 disordered side chains (Lys3, Ser5, Lys7, Ile8, Pro20, Ser25, Lys29, Pro34, Asp35, Asp36, Pro40, Glu50, Arg51, Ile52 and Glu53) and six peptide bonds (Lys7-Ile8-Cys9, Pro34-Asp35-Asp36-Trp37, Ile52-Glu53) standard geometrical restraints had to be applied to preserve a reasonable structure of the model (452 restraints). To evaluate the potential influence of a fully restrained refinement on the stereochemistry of PaRd W4L/R5S, the final round of refinement was repeated with a full set of standard restraints (1476 geometrical restraints). The differences between the partially and fully restrained models turned out to be smaller than the estimated standard uncertainties, confirming similar observations from other atomic resolution refinements (Kang et al., 2004; Esposito, Vitagliano, Sica et al., 2000).

The very high data-to-parameter ratio of 25.8 and the small size of the molecule allowed the application of an unblocked full-matrix least-squares procedure in the final rounds of refinement. The full-matrix least-squares refinement is supposed to be more accurate than the conjugate-gradient method at the cost of considerably increased computation time; however, the R_{free} value and the model were not changed. A similar observation was reported for the refinement of syntenin PDZ2 domain (Kang et al., 2004). Most importantly, the inversion of the full matrix provided proper estimates for the standard uncertainties of all refined parameters. The mean estimated standard uncertainty for fully occupied atoms was 0.007 Å for the atomic positions, 0.004 Å for the bond distances and 0.3° for the bond angles.

3.3. Protein model

The final model of PaRd WT consisted of four Rd molecules and 157 solvent molecules in the AU. Each molecule was complete and consisted of residues 1–53 and the iron ion, with

the exception of molecule C, where Met1 could not be modelled. The estimated overall coordinate error based on the R value was 0.098 Å. The r.m.s. displacement for C^α atoms 2–53 between the four molecules in the AU ranged from 0.326 to 0.572 Å, with the largest deviations for chain C (Fig. 2). The structural differences were smallest for the antiparallel β-sheet and the redox site, whereas the part between residues 15 and 37 showed differences in C^α-atom positions of up to 2 Å. As expected, the structure of PaRd WT is highly homologous to the structures of PfRd (Bau et al., 1998), CpRd (Dauter et al., 1996), DgRd (Frey et al., 1987) and DvRd (Z. Dauter, S. Butterworth, L. C. Sieker, G. Sheldrick & K. S. Wilson, unpublished work; PDB code 1rb9).

The final model of PaRd W4L/R5S was also complete and consisted of residues 2–53, the iron ion and 94 solvent molecules. The electron-density maps showed clear density for all non-H atoms with the exception of Lys7, where the side-chain atoms C^ε and N^ζ were not visible owing to rotational disorder (Fig. 3a). The model could be built without any ambiguities because atom types were identifiable by their density volume and most protons were visible. The electron-density maps provided detailed information on conformational disorder that allowed modelling of alternative conformations for 13 residues. Alternative main-chain conformations were clearly visible for Ile8 and the segment from Pro34 O to Tyr37 N. The side chain of Ile8 was involved in hydrophobic crystal contacts and adopted two alternative conformations, which also caused a slight change in main-chain conformation. Residues 34–37 form a highly flexible turn (Fig. 2) in all known Rd structures and were poorly defined in the electron-density map of PaRd WT. In PaRd W4L/R5S, two extreme positions of this flexible part could be modelled as two alternative conformations. The C-terminal residue Glu53 was not well defined and the electron density suggested the existence of an alternative position for Ile52 and Glu53 which could not be modelled properly.

The comparison between PaRd WT and W4L/R5S revealed that the W4L mutation introduced small structural changes (Fig. 4), whereas the overall structure of W4L/R5S was not affected by the mutations (Fig. 2). The r.m.s. displacement for C^α atoms 2–52 ranged between 0.632 and 0.823 Å, with the best fit for WT molecule A. The exchange of the planar side chain of Trp4, which made an aromatic stacking interaction with Phe30, by the non-planar side chain of Leu4 forced both side chains, and with them the corresponding main chains, to move apart. The main chain of β-strand 1 between residues 2 and 7 was slightly shifted, with a displacement of ~0.5 Å for C^α atoms 4, 5 and 7. β-strands 2 and 3 of the antiparallel β-sheet were moved in the same direction and these distortions were also propagated to the more flexible region between residues 15 and 37 via hydrogen bonds and hydrophobic interactions (Tyr11, Tyr13, Leu33, Trp37). As a result, small structural changes with respect
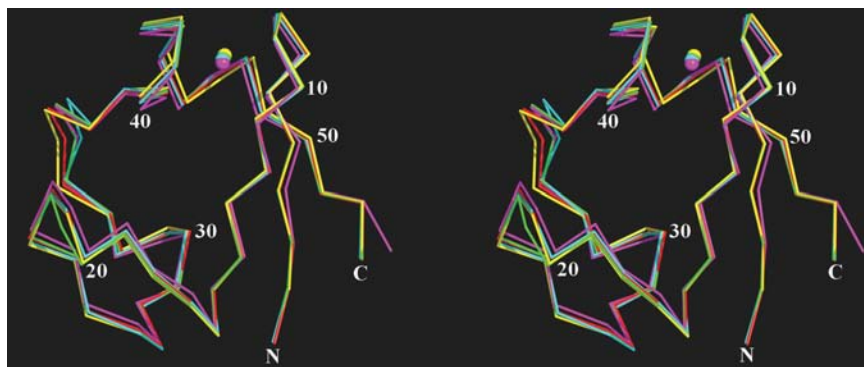

Figure 2
Stereoview of a superposition of P. abyssi rubredoxin wild type and mutant W4L/R5S. The C^α backbones of the four molecules in the asymmetric unit of the wild-type protein are shown in cyan, red, yellow and green and the C^α backbone of mutant W4L/R5S is shown in magenta. Every tenth residue and the N- and C-terminal residues are marked.

to the iron-binding site could be observed in the whole structure of PaRd W4L/R5S (Figs. 2 and 4). In addition to these structural changes induced by the W4L mutation, artificial distortions of the first metal-binding turn by crystal contacts were observed. The side chain of Ile8 was locked into two alternative conformations by hydrophobic contacts with the side chains of Tyr11 and Pro40 in a neighbouring molecule, which caused a minor deformation of the main chain (Fig. 4). Most significant was the observation of a peptide flip in residue Cys9, *i.e.* a rotation by 180° around bond Cys9 C^α—C, which moved Gly10 C^α outwards by ~2 Å and also affected Tyr11. This peptide flip was the result of a weak intramolecular
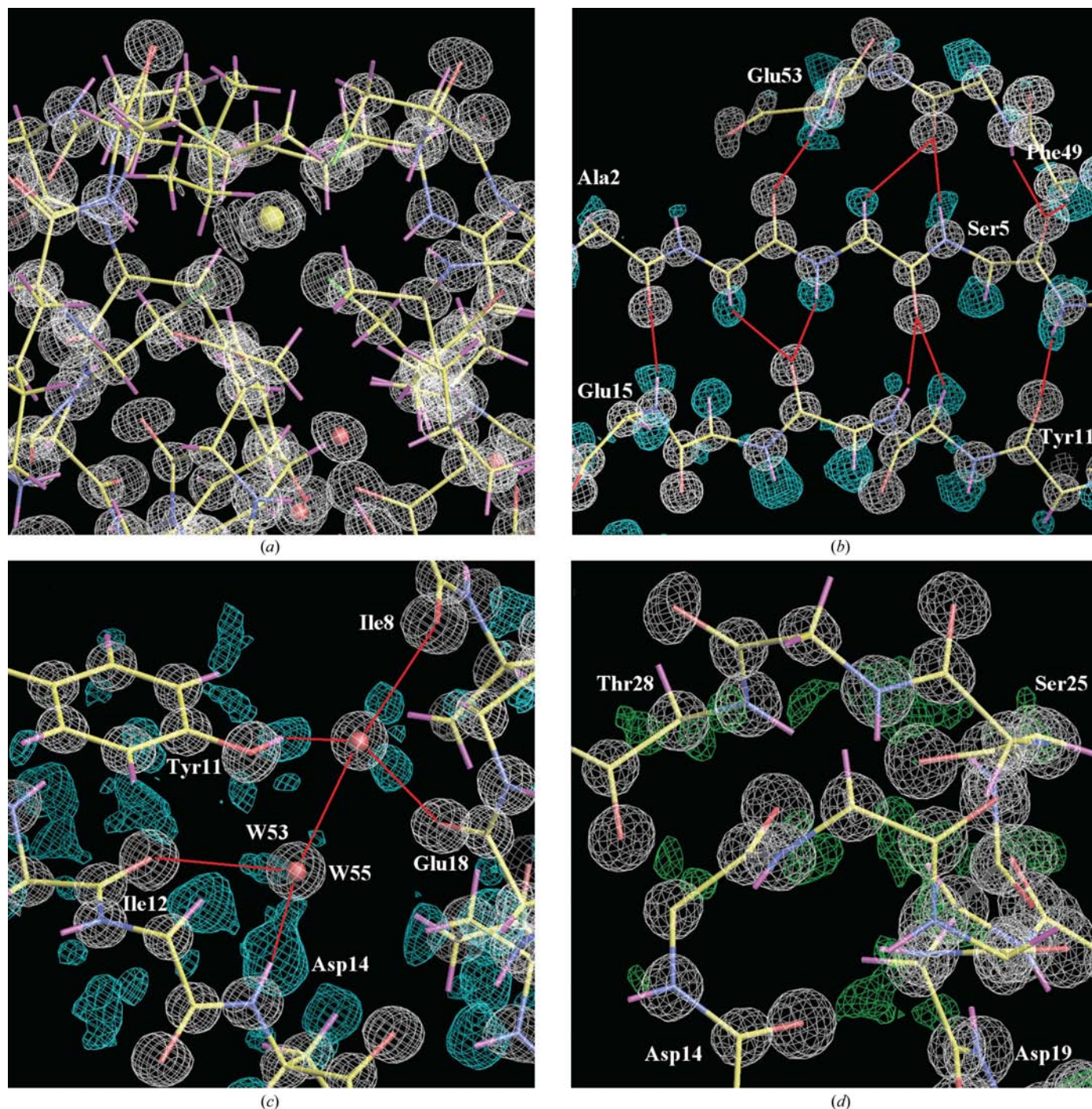

Figure 3
P. abyssi rubredoxin W4L/R5S. Electron-density maps calculated from the final model refined to 0.69 Å resolution, superimposed onto the final model. (*a*) $2mF_o - DF_c$ difference map of the redox centre; the contour level is 3.0σ. (*b*) $2mF_o - DF_c$ difference map (white; contour level 3.0σ) and proton-omit map (cyan; contour level 2.0σ) of the antiparallel β-sheet. The main chain of the final model is shown. D—H$\cdots$$A$ and C—H$\cdots$O hydrogen bonds are marked by red lines. (*c*) $2mF_o - DF_c$ difference map (white; contour level 3.0σ) and proton omit map (cyan; contour level 2.0σ) of a hydrogen-bond network with well ordered solvent molecules. The hydrogen bonds are marked by red lines. (*d*) $2mF_o - DF_c$ difference map (white; contour level 3.0σ) and $mF_o - DF_c$ difference map (green; contour level 2.0σ) for residues Asp14–Asp19 and Ser25–Thr28. The main chain of the final model is shown.

hydrogen bond between Gly10 N and Glu17 OE1 of a neighbouring molecule, which replaced the intermolecular hydrogen bond Cys6 O—Gly10 N. The second metal-binding turn between Trp37 and Lys46 showed no remarkable differences between PaRd WT and W4L/R5S, with the exception of the side-chain conformations of Pro40 and Ile41 (Fig. 4). For the latter, the occurrence of two distinct side-chain conformations has been discussed with respect to a potential function as a water gate during electron transfer (Min *et al.*, 2001).

The structural changes caused by the W4L mutation and by the crystal contacts did not severely affect the geometry of the $Fe(SCys)_4$ centre (see below). Although they imposed some strain on the structure, *e.g.* on the peptide bond Ser5-Cys6, the C^α atoms and side chains of the four cysteine ligands were kept in place by their strong interactions with the iron ion.

3.4. Stereochemistry

The partially restrained ultrahigh-resolution refinement of PaRd W4L/R5S provided very precise stereochemical data. Bond distances and angles from well ordered residues with low estimated standard uncertainties were used for a detailed stereochemical analysis of the peptide-backbone geometry. A statistical analysis of side-chain conformations was not performed because of the small size of the molecule.

This analysis of the peptide-backbone geometry revealed features that were in line with recently published results from the statistical analysis of structural databases and individual atomic resolution structures. Most obvious were deviations from peptide-bond planarity owing to a bond twist around the C—N bond. For PaRd W4L/R5S the mean ω angle for 51 peptide bonds of the main conformer was 178.7°, with a standard deviation of 6.4° (Fig. 5a). These values were in good agreement with a mean value of 179.0° and a standard deviation of 5.9° found for atomic resolution structures by MacArthur & Thornton (1996). Unusually large deviations from planarity were observed for eight peptide bonds. The movement of β-strand 1 against the fixed ligand residue Cys6 caused deformation of peptide bond Ser5-Cys6 ($\omega = 165°$), whereas Lys7a-Ile8a ($\omega = 199°$) was affected by the involvement of Ile8 in crystal contacts. Glu17-Gly18 ($\omega = 192°$), Asp19-Pro20 ($\omega = 194°$), Ser25-Pro26 ($\omega = 168°$) and Asp36a-Trp37 ($\omega = 169°$) were all located in flexible parts at the beginning or end of secondary-structure elements. Peptide bond Leu41-Cys42 was strained by crystal contacts of Leu41 ($\omega = 189°$), whereas Ile52-Glu53 belongs to the disordered C-terminus ($\omega = 168°$).

The mean values for peptide-backbone bond distances and angles were in good agreement with the values derived from the crystallographic analysis of peptide-backbone fragments (Engh & Huber, 2001). However, for several individual bonds significant deviations from these standard values were observed, which in some cases could be explained by strain introduced by the W4L mutation and crystal contacts (results not shown).

In several atomic resolution structures of very high quality a negative correlation between peptide C—O and C—N bond

lengths was observed in accordance with the classical amide-resonance model (Howard *et al.*, 2004; Esposito, Vitagliano, Zagari *et al.*, 2000b). This phenomenon was also observable in the structure of PaRd W4L/R5S when 14 peptide bonds with equivalent isotropic B factors below 4 $Å^2$ and a mean standard uncertainty of 0.0034 Å for C—O and C—N bond lengths were analyzed: length C—O (Å) = 1.88 Å $-$ 0.48 × length C—N (Å); $R = 0.47$ (Fig. 5b).

Furthermore, most backbone carbonyl groups showed a slight deviation from planarity, the so-called pyramidalization of the carbonyl C atom, which can be described by the angle θ_c between the planes $C_i^\alpha C_i N_{i+1}$ and $N_{i+1} C_i O_i$ (Esposito, Vitagliano, Zagari *et al.*, 2000a). θ_c was calculated as the difference between torsion angles ω and ω_3: $\theta_c = \omega(C_i^\alpha C_i N_{i+1} C_{i+1}^\alpha) - \omega_3(O_i C_i N_{i+1} C_{i+1}^\alpha) + 180°$. The analysis of 35 peptide bonds with a mean standard uncertainty below 0.5° for ω and ω_3 resulted in θ_c values between -5.21 and 3.41°. In a plot of θ_c against torsion angle Ψ, a correlation between the carbonyl carbon pyramidalization and the conformation at the adjacent C^α atom was observed as described by Esposito, Vitagliano, Zagari *et al.* (2000a). θ_c adopts preferentially positive values (mean value = 0.6°; SD = 2.1°) for residues in helical conformations (ψ values between -60 and 30°) and preferentially negative values (mean value = $-1.7°$; SD = 2.1°) for residues in extended conformations (ψ values between 110 and 180°) (Fig. 5c).

Analysis of 39 residues revealed a significant correlation between the N—C^α—C backbone angle and the corresponding Ψ torsion angle (mean standard uncertainty for N—C^α—C angle 0.24°, φ angle 0.33°, ψ angle 0.35°). In a plot of N—C^α—C backbone angles *versus* Ψ torsion angles two significantly different populations of N—C^α—C angles were observed, one with a mean value of 109.2° (SD = 1.7°) for residues in extended structures (ψ values between 110 and 180°) and a second with a mean value of 113.5° (SD = 1.6°) for
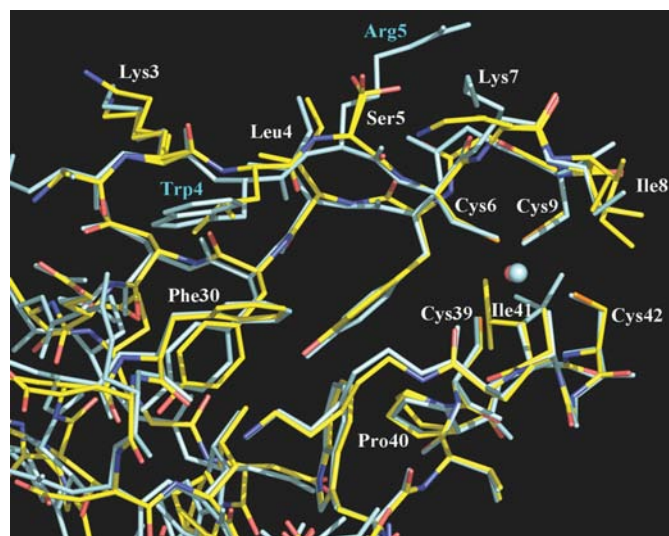

Figure 4
P. abyssi rubredoxin wild-type molecule *A* (cyan) and mutant W4L/R5S (atom colours). Superposition of the $Fe(SCys)_4$ site.

residues in α-helical or loop regions (ψ values between -45 and $60°$) (Fig. 5d). Only a weak approximately linear correlation was observed between the $N-C^\alpha-C$ angles and torsion angle φ (Esposito *et al.*, 2002; Esposito, Vitagliano, Sica *et al.*, 2000; Karplus, 1996).

3.5. Geometry of the Fe(SCys)$_4$ centre

The ultrahigh-resolution structure of PaRd W4L/R5S provides the most precise model of an oxidized Fe(SCys)$_4$ centre available so far (Table 3). The high precision facilitates the comparative analysis of redox-site geometries between different Rds, because random errors in the structure-determination process are very small and negligible. Thus, under the assumption that gross systematic errors are absent or at least affect compared structures in the same way, differences between models refined to ultrahigh resolution should reflect real structural differences. As an example, the comparison of PaRd W4L/R5S and PfRd reveals small differences in Fe—S bond distances and angles, which are significantly larger than the estimated standard uncertainties calculated for both structures. The reliable analysis of even such small structural deviations may be of some importance, because the electron-transfer process and the fine tuning of the redox potential are known to be connected to subtle structural changes (Park, Eidsness *et al.*, 2004; Day *et al.*, 1992). With respect to PaRd W4L/R5S, the most interesting question was whether the W4L/R5S mutation significantly influenced the geometry of the Fe(SCys)$_4$ centre and its redox potential. The observation of a slightly decreased redox potential (see below) led to the conclusion that the W4L/R5S mutation must have caused some structural changes in the Fe(SCys)$_4$ site or its environment. Comparison showed that the overall geometry of the Fe(SCys)$_4$ centre was well conserved in PaRd
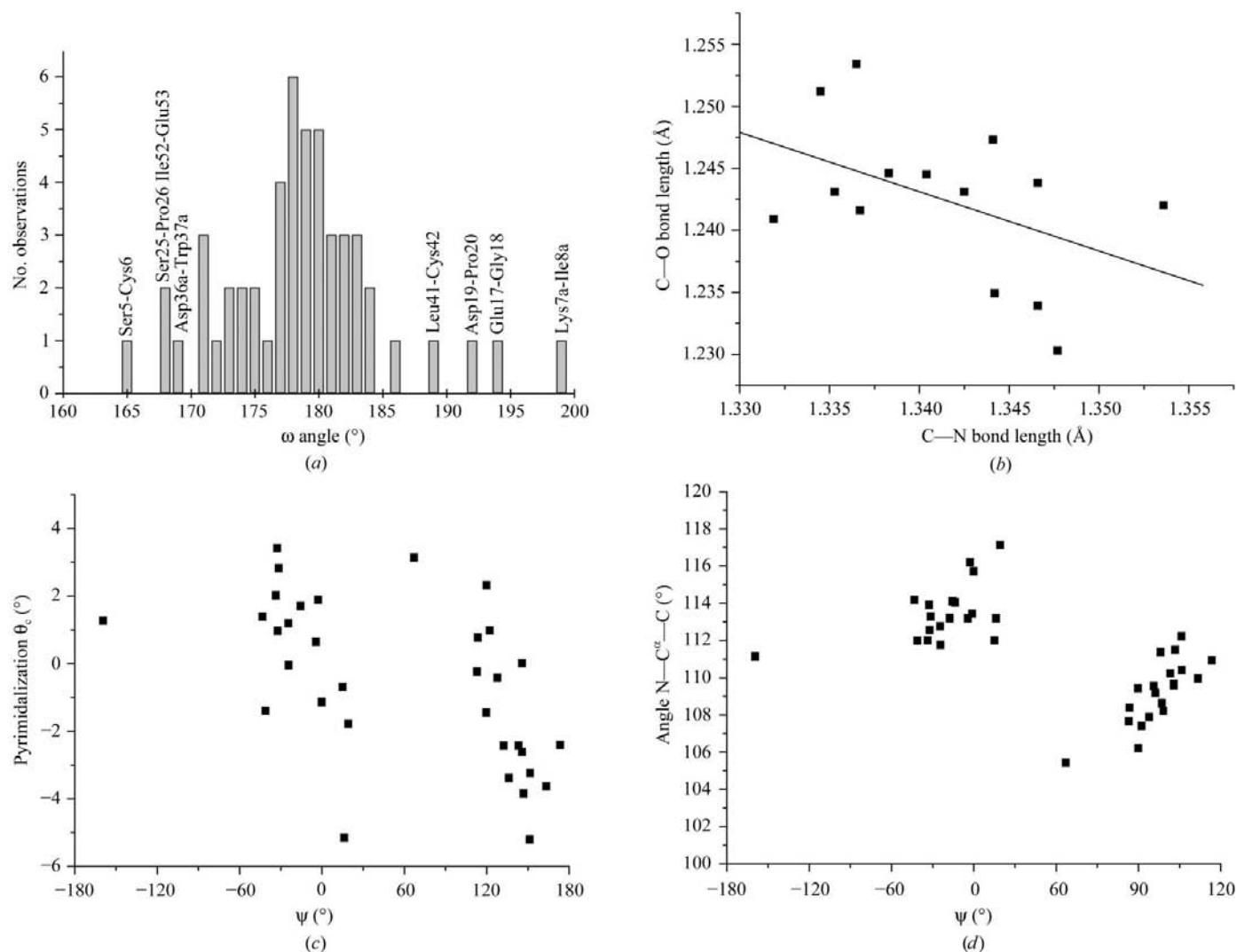

Figure 5
Stereochemistry of the peptide backbone for *P. abyssi* rubredoxin mutant W4L/R5S. (*a*) ω-angle distribution for 51 peptide bonds of the main conformer. Eight peptide bonds with large deviations from $180°$ are marked (see text). (*b*) Correlation between C—O and C—N bond lengths for 14 selected peptide bonds. The line represents a least-squares fit to the data (see text). (*c*) Correlation between the carbonyl C atom pyramidalization angle θ_c for 35 selected peptide bonds and the torsion angle Ψ. (*d*) Plot of bond angle $N-C^\alpha-C$ against torsion angle Ψ.

Table 3
Distances and angles for the oxidized Fe(SCys)$_4$ site.

Residue†	P. abyssi WT					P. abyssi W4L/R5S	P. furiosus			D. vulgaris
	A	B	C	D	Mean					
Diffraction	X-ray, 1.79 Å					X-ray, 0.69 Å	X-ray, 0.95 Å‡	X-ray, 1.80 Å§	Neutron, 1.50 Å¶	X-ray, 0.92 Å††
PDB code	1yk5					1yk4	1brf	1caa	1vcx	1rb9
Fe—S distances (Å) and angles (°)										
Fe—(Cys6)	2.30	2.31	2.24	2.28	2.28	2.2946 (21)‡‡	2.283 (3)‡‡	2.31	2.24	2.28
Fe—(Cys9)	2.22	2.28	2.23	2.23	2.24	2.2726 (18)	2.248 (3)	2.25	2.25	2.27
Fe—(Cys39)	2.31	2.29	2.27	2.26	2.28	2.3330 (15)	2.297 (3)	2.33	2.24	2.29
Fe—(Cys42)	2.21	2.20	2.29	2.28	2.24	2.2771 (21)	2.259 (3)	2.25	2.25	2.24
(Cys6)—Fe—(Cys9)	115.69	115.75	115.91	114.79	115.54	117.48 (4)	113.4 (1)	113.36	116.79	114.86
(Cys6)—Fe—(Cys39)	112.19	111.13	111.73	112.43	111.87	110.7 (1)	110.7 (1)	111.98	105.13	110.51
(Cys6)—Fe—(Cys42)	104.36	105.60	104.55	104.38	104.72	103.41 (5)	103.8 (1)	102.60	103.78	105.05
(Cys9)—Fe—(Cys39)	100.82	100.56	100.59	101.27	100.81	99.38 (7)	102.4 (1)	102.20	104.62	104.26
(Cys9)—Fe—(Cys42)	111.50	110.45	111.95	110.17	111.02	113.97 (6)	114.3 (1)	115.05	118.47	110.49
(Cys39)—Fe—(Cys42)	112.61	113.63	112.40	114.12	113.19	112.09 (5)	112.6 (1)	112.03	106.99	111.84
N—H···S hydrogen bonds§§										
Ile8 N/Cys6 S	3.54	3.54	3.55	3.53	3.55	3.49 (2.66; 157.82)	3.60	3.52	3.75 (2.94; 140.67)	3.55
Cys9 N/Cys6 S	3.62	3.61	3.62	3.58	3.61	3.65 (2.97; 135.97)	3.69	3.58	3.75 (2.86; 157.63)	3.57
Tyr11 N/Cys9 S	3.60	3.56	3.57	3.53	3.57	3.44 (2.58; 166.38)¶¶	3.51	3.47	3.51 (2.57; 159.41)†††	3.47
Ile41 N/Cys39 S	3.59	3.63	3.69	3.61	3.63	3.51 (2.68; 156.74)	3.53	3.42	3.59 (2.76; 146.21)	3.56
Cys42 N/Cys39 S	3.69	3.67	3.72	3.60	3.67	3.54 (2.70; 160.98)	3.62	3.52	3.57 (2.62; 178.60)	3.61
Ala44 N/Cys42 S	3.58	3.58	3.58	3.51	3.56	3.59 (2.80; 149.55)	3.53	3.49	3.46 (2.52; 159.16)	3.50

† Numbering for PaRd. ‡ Bau *et al.* (1998). § Day *et al.* (1992). ¶ Kurihara *et al.* (2004). †† Z. Dauter, S. Butterworth, L. C. Sieker, G. Sheldrick & K. S. Wilson, unpublished work. ‡‡ Estimated standard uncertainties in parentheses; estimated standard uncertainties for atomic positions in PaRd W4L/R5S: Fe 0.0006 Å, Cys S$^\gamma$ 0.001 Å. §§ D···A distances in Å; D—H···A distances and D—H···A angles in parentheses if observable. ¶¶ Hydrogen bond distorted by crystal contact. ††† Proton not observable owing to partial H/D exchange.

W4L/R5S (Table 3) and all features described for high-resolution structures of Rd iron–sulfur cores were observable, including the asymmetry in Fe–S bond lengths and bond angles (Bau *et al.*, 1998). However, small differences were observed between PaRd W4L/R5S, PaRd WT and the atomic resolution structures of PfRd and DvRd which could be of some significance; for example, the increased values for bond length Fe—Cys39 and bond angle Cys6—Fe—Cys9 in PaRd W4L/R5S. However, it was not possible to decide which of these changes were the results of the W4L/R5S mutation and possibly responsible for the modification of the redox potential and which were the consequence of differences in crystal packing, the data-collection conditions and the structure-determination process. The four molecules in the AU of PaRd WT showed variations in their bond distances and angles of comparable magnitude as a consequence of different crystal contacts. Considerable differences were also observed between three structures of PfRd obtained from the same crystal type by X-ray or neutron diffraction at different temperatures and refined to different resolution. Thus, while X-ray crystallographic refinement at ultrahigh resolution itself can provide very precise geometrical data for the iron–sulfur core, in comparative analyses attention has to be paid to the reproducibility of experimental parameters in order to exploit the full power of the method.

3.6. Spectroscopy

The oxidized and reduced Fe(SCys)$_4$ site of PaRd W4L/R5S was investigated by EPR, Mössbauer and EXAFS spectroscopy (Wegner *et al.*, 2004). EXAFS spectroscopy provided an averaged Fe—S distance of 2.33 ± 0.02 Å for the reduced and 2.28 ± 0.02 Å for the oxidized protein, which is in excellent agreement with the average Fe—S distance of 2.294 Å for the oxidized protein calculated from the ultrahigh-resolution X-ray structure.

3.7. H atoms

In the final model of PaRd W4L/R5S, 448 H atoms were placed on stereochemically predicted positions: 290 H atoms with full occupancy and 158 H atoms with occupancy below unity bound to atoms with alternative positions. The presence and the positions of the H atoms were examined in an $F_o - F_c$ difference map calculated from the final model with H atoms omitted (OMIT _* $H). Using a limit of 1σ for the residual electron density, 310 H atoms were observable in the difference Fourier map. This corresponds to 69% of all possible H atoms, compared with values of around 50% reported for other high-resolution structures, *e.g.* PfRd (~50%; 0.95 Å; Bau *et al.*, 1998), human aldose reductase (54%; 0.66 Å; Howard *et al.*, 2004) and ribonuclease A (46%; 0.87 Å; Esposito, Vitagliano, Sica *et al.*, 2000). 88% of the H atoms with full occupancy were observable, providing a level of detail comparable with the results of neutron diffraction experiments at lower resolution (Kurihara *et al.*, 2004; Chatake *et al.*, 2004). The exact localization of H atoms by X-ray diffraction is difficult even at ultrahigh resolution because the electron-density peak is often not centred at the position of the nucleus. Although the very high observation-to-parameter ratio allowed the refinement of H-atom positions in PaRd W4L/R5S as in small-molecule crystallography, test refinements led to incorrect positions for many H atoms with bond distances and angles that were not chemically

meaningful (results not shown). For this reason, the H-atom positions were refined as usual by riding H-atom constraints as implemented in *SHELXL*. However, the quality of the data allowed the refinement of torsion angles for the terminal $-NH_3^+$ group, $-CH_3$ groups, the $-OH$ groups of Ser5, Ser25, Ser47, Tyr11, Tyr13 and Thr28 and the $-NH_3^+$ group of Lys46. For Ser5 and Ser25, which showed three alternative side-chain conformations, the H-atom positions for the two most populated conformations were clearly observable. The availability of such detailed experimental data about the H-atom structure is of great importance for a reliable analysis of hydrogen-bonding interactions in the molecule.

In most cases, the stereochemically predicted H-atom positions coincided well with the corresponding peaks of the H-atom omit map. However, in some cases deviations were clearly observed. For several very well defined backbone amide protons (B factor < 4.0 Å^2) that were involved in strong hydrogen bonds, the electron-density peak was found up to 0.4 Å away from the predicted position, lying close to the line connecting hydrogen donor and hydrogen acceptor (for example, Tyr13 H0; Fig. 3b). Thus, the centre of the electron cloud and possibly even the nucleus of the H atom were moved out of the $C-N-C^\alpha$ plane by the strong hydrogen-bond interactions.

For an optimal refinement against X-ray diffraction data, the default $X-H$ bond distances used by *SHELXL* are shorter than the true internuclear distances. The $X-H$ bonds in PaRd W4L/R5S were on average 0.1 Å shorter than those used for the refinement of PfRd against neutron diffraction data (Kurihara *et al.*, 2004; Chatake *et al.*, 2004), which has consequences for the analysis of hydrogen-bond distances and energies (see below; Table 3). An alternative approach is to refine a model with $X-H$ bond distances taken from neutron scattering data, which would introduce a systematic error during refinement against X-ray data and produce residual electron density along the $X-H$ bonds (Afonine *et al.*, 2004), or to refine with default $X-H$ bonds and to use bond distances from neutron scattering for the construction of the final model.

3.8. Hydrogen bonds

Hydrogen bonds play an important role in the stability of Rd as well as for the adjustment of the redox potential. The experimental observation of H atoms in atomic resolution X-ray structures and medium-resolution neutron diffraction structures allows a comprehensive and reliable analysis of these hydrogen-bond interactions, especially for titratable and freely rotating groups for which the presence and positions of H atoms are not predictable.

Taking a maximal $D-H\cdots A$ distance of 3.0 Å and a $D-H\cdots A$ angle of at least $90°$ as cutoff criterion (Desiraju & Steiner, 1999), 53 intramolecular hydrogen bonds were found in PaRd W4L/R5S based on the predicted positions of the riding H atoms. The presence of 46 hydrogen bonds could be confirmed experimentally in the H-atom omit map, 29 of 31 main chain–main chain, eight of 12 side chain–main chain,

three of five side chain–side chain and all six $N-H\cdots S$ hydrogen bonds. Torsion-angle refinement of Tyr13 OG, Thr28 OG, Lys46 NZ and Ser47 OG allowed the assignment of five of these hydrogen bonds. Two hydrogen bonds were not experimentally observable because of main-chain disorder (Ile9, Asp36) and four because of rotational disorder of side chains (Ser5, Lys3, Lys7, Lys29). The hydrogen bond between Gly10 N and Cys6 was disrupted by the peptide flip around Cys9 $C^\alpha-C$ and was replaced by an artificial hydrogen bond between Tyr11 N and Cys9 O. In the antiparallel β-sheet, six secondary $C-H\cdots O$ hydrogen bonds were experimentally observable when a cutoff of 3.5 Å for the $C^\alpha\cdots O$ distance and $130°$ for the $C^\alpha-H\cdots O$ angle was applied (Fabiola, 1997) (Fig. 3b).

As expected from the high structural similarity, the hydrogen-bonding network of PaRd W4L/R5S was nearly identical to the hydrogen-bonding network in PfRd. Analysis of the PfRd neutron diffraction structure (Kurihara *et al.*, 2004) using the same cutoff criteria revealed the presence of five additional hydrogen bonds, two arising from differences in sequence (W4L, E32D) and three arising from differences in conformation (Glu30, Glu47, Glu52). The most interesting difference was the lack of hydrogen bond Trp NE1–Glu15 OE1 in PaRd W4L/R5S caused by the W4L mutation. This hydrogen bond is part of a hydrogen-bond network around the N-terminus whose influence on thermostability has been discussed in detail for PfRd (Chatake *et al.*, 2004). However, at present no experimental data are available on the potential effect of this mutation on the thermostability of PaRd W4L/R5S.

The detailed analysis of hydrogen bonds between backbone amide protons and the four Cys S^γ atoms is of special interest because they seem to have an important influence on the redox potential in rubredoxins and iron–sulfur proteins in general. For the 1.8 Å structure of PfRd, six $N-H\cdots S$ hydrogen bonds were assigned in the original publication (Day *et al.*, 1992). This list was extended by an additional three hydrogen bonds by Bau *et al.* (1998) for the 0.95 Å structure. Using H-atom positions experimentally observable by neutron diffraction, five of the six original hydrogen bonds were confirmed (one H atom was not observable owing to partial H/D exchange), whereas the additional three hydrogen bonds assigned by Bau *et al.* (1998) were refuted because they showed large $D\cdots H$ distances (>3.0 Å) and small $D-H\cdots A$ angles ($<90°$) (Kurihara *et al.*, 2004; Table 3). In the PaRd W4L/R5S structure all H atoms involved in potential $N-H\cdots S$ hydrogen bonds were very well defined, with the exception of Cys9 H0, which had a weaker density because of partial occupancy. In this way, it was possible to confirm the presence of all six $N-H\cdots S$ hydrogen bonds assigned by Day *et al.* (1992) and to obtain precise data about the binding geometry (Table 3).

In summary, this ultrahigh-resolution structure provided a very detailed model of the hydrogen-bonding network of PdRd, which will provide the basis for a detailed comparative analysis of $D-H\cdots A$ and $N-H\cdots S^\gamma$ hydrogen bonds in different mutants.

3.9. Solvent structure

The ultrahigh-resolution σ_A-weighted $2F_o - F_c$ and $F_o - F_c$ difference maps provided very detailed information about the solvent structure, but not all observed features could be modelled in order to keep the *SHELXL* refinement stable. The final model contained 94 water sites, 22 of which had half occupancy. 75 sites belonged to the first solvent shell, forming at least one hydrogen bond with a protein atom, and 19 belonged to the second solvent shell. Interestingly, the average isotropic B factor for water molecules in both shells was approximately the same: 18 and 19 Å^2, respectively. On one hand, part of the visible second solvent shell was still very well defined by strong hydrogen-bond networks. On the other hand, many of the solvent molecules in the first solvent shell showed clear disorder, either in the form of discrete alternative positions or in the form of thermal displacement parallel to the protein surface, which could not be modelled adequately and lead to increased isotropic B factors. In the $2F_o - F_c$ map an 22 itional water sites with peak density above 1σ and reasonable hydrogen bonding could be identified which did not behave well during refinement.

With a solvent space of 15 218 Å^3 and a volume of approximately 30 Å^3 per water molecule (Bau *et al.*, 1998), a total of 127 water molecules per Rd molecule can be expected. Thus, approximately 90% of the solvent molecules were visible in the density, 75% could be included in the refined model and about 25% had to be treated as diffuse solvent.

For several very well defined water molecules with low B factors (<5 Å^2) in an $F_o - F_c$ difference map spherical peaks were observable in the direction of hydrogen bonds, indicating the positions of water H atoms and allowing the precise assignment of hydrogen bonds (Kang *et al.*, 2004; Fuhrmann *et al.*, 2004). An example is presented in Fig. 3(*c*): it shows a small hydrogen-bond network between two neighbouring PaRd W4L/R5S molecules involving two water molecules, three carbonyl O atoms (Ile8, Ile12, Gly18), one main-chain amide H atom (Asp14) and the H atom of a tyrosine side chain (Tyr11). All six H atoms involved in this network were clearly visible in the difference Fourier map that permitted the direct assignment of all hydrogen bonds.

The construction of a complete and detailed model of the solvent space is of importance because of the suggested participation of solvent molecules in the electron-transfer mechanism and the influence of the solvent accessibility of the redox site on the redox potential (Park, Youn *et al.*, 2004).

3.10. Thermal displacement

The refinement of anisotropic atomic displacement parameters (ADPs) for non-H protein and water O atoms in PaRd W4L/R5S provided detailed information about static and dynamic disorder in the crystal. During the *SHELXL* refinement the anisotropic ADPs of protein atoms and solvent molecules were not restrained, with exception of the components of the anisotropic ADPs in the direction of covalent bonds, which were restrained by a rigid-bond restraint (*SHELXL* command DELU). The analysis of ADPs with

PARVATI (Merritt, 1999) yielded a mean anisotropy of 0.449 ($\sigma = 0.183$) for protein atoms and 0.420 ($\sigma = 0.189$) for all atoms (Table 2). This distribution is similar to a typical distribution (mean value of 0.45; $\sigma = 0.15$) determined from an analysis of 67 protein structures (Merritt, 1999) and the distributions for three Rd structures for which anisotropic ADPs have been deposited (PDB codes 1iro, 1irn and 1rb9). As expected, the most anisotropic displacements were observed for disordered side chains of surface residues and the C-terminus, whereas atoms in the hydrophobic core showed the most isotropic displacements (Fig. 6*a*). In comparison with the three Rd structures mentioned above, the distribution of anisotropy for the solvent molecules of PaRd W4L/R5S was skewed towards higher anisotropy, with a significantly lower mean value of $A = 0.275$ ($\sigma = 0.143$). For a larger number of water molecules a strong thermal movement parallel to the protein surface was observed in the electron density, which could not be modelled properly by alternative solvent positions (Fig. 6*b*). This lead to strongly anisotropic ADPs during refinement, because the ADPs of the solvent molecules were not restrained to be approximately isotropic (*SHELXL* command ISOR).

3.11. Deformation density

At ultrahigh resolution, the deviation of the real electron-density distribution from the spherical or ellipsoidal atomic model used in refinement becomes visible. In several recent ultrahigh-resolution structures difference electron-density peaks have been observed in the middle of individual bonds in well ordered parts of the structure (Jelsch *et al.*, 2000; Ko *et al.*, 2003; Howard *et al.*, 2004). Afonine *et al.* (2004) showed in a detailed study that deformation density (bond electron density) could be observed in conventional $F_o - F_c$ residual maps for well ordered individual residues when the average isotropic B factors were below ~5 Å^2 and if the phases were calculated from a model refined to ultrahigh resolution (close to 0.6 Å). In accordance with the results of this study, deformation density was visible in the 0.69 Å structure of PaRd W4L/R5S (average main-chain B factor 4.83) around a limited number of individual atoms with an equivalent isotropic B factor below 4 Å^2. In an $F_o - F_c$ difference Fourier map calculated for the final model of PaRd W4L/R5S, bond electron density was observed for approximately 60 covalent bonds (Fig. 3*d*). Most clearly observable were bond electrons along main-chain $C^\alpha-C$ bonds. For several main-chain N atoms and O atoms difference density resulting from the partial double-bond character of the peptide bond and the free electron pair of the carbonyl O atom could be observed. In approximately ten side chains deformation density for the $C^\alpha-C^\beta$ bond was visible.

As pointed out by Afonine *et al.* (2004), Fourier syntheses for ultrahigh-resolution data may produce artificial density owing to Fourier truncation effects, especially in unbalanced $mF_o - nF_c$ electron-density maps. For the PaRd W4L/R5S structure, strong ripples around the Fe^{3+} ion and the four ligand S$^\gamma$ atoms were observed in a σ_A $2mF_o - DF_c$ difference
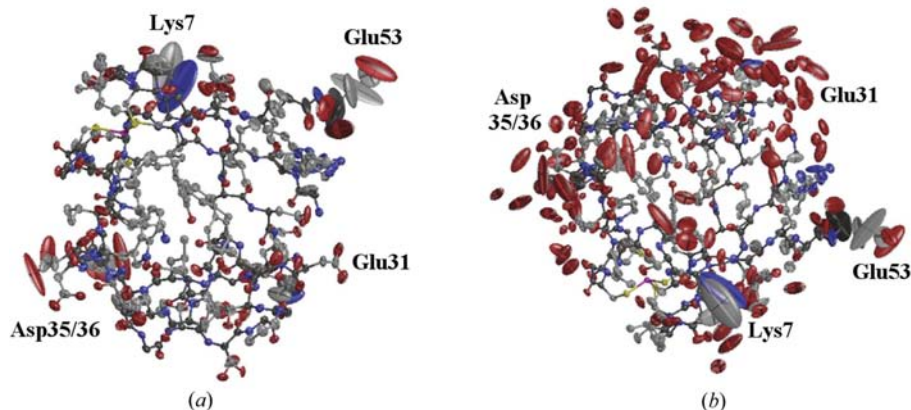
Figure 6
Anisotropic atomic displacement of *P. abyssi* rubredoxin mutant W4L/R5S. 50% probability thermal ellipsoids are shown (*PARVATI*; Merritt, 1999). (*a*) Protein only, (*b*) protein and solvent.

map (Fig. 3*a*) and less prominently in an $F_o - F_c$ map below an electron-density level of 0.15 Å^{-3}. Apart from these density ripples, no prominent residual density was observed for the Fe(SCys)$_4$ centre.

The analysis of deformation density provides very precise information about the electron distribution in a molecule, which in turn can be used for example for calculations of electrostatic potentials and the assessment of *in situ* reactivity (Howard *et al.*, 2004). For the PaRd mutagenesis project it would be very interesting to analyze the effect of different mutations on the electron distribution in the vicinity of the Fe(SCys)$_4$ site. However, although deformation density was observable in individual cases, the quality of the bond electron density directly observable in a conventional $F_o - F_c$ difference map of PaRd W4L/R5S did not seem to be sufficient to provide this information. Instead, it seems to be more promising to monitor changes in the electron distribution by charge-density refinement with a multipolar model (Guillot *et al.*, 2001) or indirectly by their influence on the binding parameters of covalent bonds.

3.12. Redox potential

A value of −18 mV was determined for the redox potential of PaRd WT by cyclic voltammetry, whereas −36 mV was measured for PaRd W4L/R5S. Thus, the W4L/R5S mutation caused a small but significant decrease in the redox potential. It has been suggested that the redox potential of Rd can be modified by changes in the ligand sphere of the Fe(SCys)$_4$ centre as well as by changes in its local environment involving peptide dipoles, polar side chains, N−H···S hydrogen bonds and solvent molecules (Park, Eidsness *et al.*, 2004; Swartz *et al.*, 1996; Eidsness *et al.*, 1999). The W4L mutation in the hydrophobic core caused small changes in the W4L/R5S structure which could have effects on the geometry of the Fe(SCys)$_4$ site, the bond lengths of N−H···S hydrogen bonds and the distances between peptide dipoles and the iron ion. Analysis of the Fe(SCys)$_4$ centre revealed small deviations in geometry, which, however, could not be linked unambiguously to the W4L mutation owing to significant differences in crystal

packing and data-collection conditions between PaRd WT and W4L/R5S. The same was observed for the bond lengths of N−H···S hydrogen bonds and the distances between the iron ion and the peptide dipoles (Table 3). Mutagenesis experiments in CpRd revealed a strong correlation between the redox potential and the length of the N−H···S hydrogen bond between residue 44 and Cys42, where a shortening of this distance by up to 0.6 Å was correlated with an increase of the redox potential by a maximum of 100 mV (Park, Eidsness *et al.*, 2004; Lin *et al.*, 2003). When the bond lengths of five N−H···S hydrogen bonds in PaRd W4L/R5S were compared with the mean values for PaRd WT, three N−H···S hydrogen bonds were found to be shortened by up to 0.11 Å, while two hydrogen-bond distances were increased by up to 0.06 Å (Table 3). Thus, the theoretically expected increase in N−H···S hydrogen-bond lengths and iron–peptide dipole distances could not be observed and the small differences found were again comparable to the magnitude of variation caused by experimental parameters.

The R5S mutation on the molecular surface did not change the structure of the protein molecule, but could theoretically influence the electrostatic potential at the Fe(SCys)$_4$ site and its solvent-accessibility. According to Coulombic electrostatics, the presence of a positive surface charge close to the Fe(SCys)$_4$ centre should help to stabilize the additional negative charge in the reduced state. Thus, the replacement of the positively charged side chain of Arg5 by serine could contribute to the observed decrease in redox potential. The effects of changed surface charges on the redox potential were investigated in several experimental studies, but the results were inconsistent and in many cases not interpretable by simple electrostatic interactions alone (Kuemmerle *et al.*, 1997; Zeng *et al.*, 1996). In this context, it was most interesting that a T5R/T7R double mutation in CpRd increased the redox potential by only 5 mV (Zeng *et al.*, 1996), whereas the introduction of arginine residues closer to the iron site (V8R, L41R, V8R/L41R) caused a significant increase in redox potential by 40, 58 and 85 mV, respectively. This suggested that the potential effect of the R5S mutation on the electrostatic potential at the Fe(SCys)$_4$ site of PaRd W4L/R5S might be rather small because of the large distance of ~10 Å (Fig. 4).

The solvent-accessibility of the redox site is also considered as an important parameter for the redox potential. The redox potential should be increased by better solvent accessibility, because the more highly charged reduced state of the Fe(SCys)$_4$ site is better stabilized by a more polar environment compared with the oxidized state. Accordingly, in CpRd the mutation L41A caused an increase of the redox potential by ~50 mV, which was correlated to facilitated water access to Cys9 in the reduced state (Park, Youn *et al.*, 2004). The unexpected increase of the redox potential after introduction

of electrostatically unfavourable aspartate residues close to the $Fe(SCys_4)$ site of CpRd (V8D, L41D) was also explained by improved solvent access through better solvated charged side chains (Zeng *et al.*, 1996). For PaRd, no indices for an effect of the W4L/R5S mutation on the solvent-accessibility to the $Fe(SCys_4)$ centre were found, but the analysis was seriously hampered by the differences in crystal packing and the lack of structures for the reduced enzymes. Owing to the large distance to the $Fe(SCys_4)$ site, is it rather unlikely that this mutation had a significant effect on the solvent-accessibility of the iron–sulfur centre, which is in agreement with the results for the (T5R, T7R) variant of CpRd (Zeng *et al.*, 1996).

In summary, the structural information available did not allow us to draw clear conclusions about the structural basis for the change in the redox potential. The measured shift in redox potential was quite small and very likely correlated to small structural changes which could not be discriminated from the effects of experimental parameters such as crystal packing, data-collection conditions and model precision. The most likely mechanism was a change of the local environment of the $Fe(SCys_4)$ centre by the rearrangements caused by the W4L mutation. To resolve this issue, additional mutagenesis experiments are in progress.

4. Conclusions

The aim of this project is to investigate possible mechanisms for the redox potential fine-tuning in iron–sulfur proteins using *P. abyssi* rubredoxin as a model system. One general approach in this kind of study is to correlate structural differences in naturally occurring or designed variants of iron–sulfur proteins with observed differences in redox potentials. This requires the availability of high-quality X-ray structures, because experimental evidence has shown that the adaptation of the redox potential is accomplished by very small structural changes in the immediate environment of the iron–sulfur site. Thus, accurate data on the geometry of the iron–sulfur centre, on hydrogen bonding, dipole–dipole interactions and the solvent structure are needed for a reliable comparative analysis.

The structure of *P. abyssi* rubredoxin mutant W4L/R5S refined to 0.69 Å described in this work represents the most precise model of an oxidized rubredoxin available thus far and fulfils the requirements listed above. The high quality of the electron-density map allowed the construction of a complete protein model including main-chain and side-chain disorder. Experimentally observable H-atom positions provided an almost complete picture of the hydrogen-bonding interactions in the molecule. The structure of the $Fe(SCys_4)$ centre and its binding site was determined with very high precision, which facilitates the detection of changes in the ligand sphere and in non-covalent interactions with the environment. The electron-density maps provided a detailed and almost complete picture of the solvent space, which allows investigation of the influence of the solvent on electron transfer and redox potential. The visibility of deformation density and the availability of

high-quality stereochemical data provide the opportunity to monitor directly or indirectly changes in the electron distribution around the $Fe(SCys_4)$ site. Altogether, the ultrahigh-resolution structure of PaRd W4L/R5S is a very good starting point for the site-directed mutagenesis project outlined above, with the possibility of employing additional methods such as charge-density refinement and quantum-chemical calculations. Several mutants were constructed based on PaRd W4L/R5S, for which structure solution at atomic and ultrahigh resolution is in progress and where special attention is paid to the reproducibility of experimental parameters. It is expected that the comparative analysis will contribute to the understanding of the correlation between structure, redox potential and spectroscopic properties in rubredoxins and iron–sulfur proteins in general.

References

Afonine, P. V., Lunin, V. Y., Muzet, N. & Urzhumtsev, A. (2004). *Acta Cryst.* D**60**, 260–274.

Bau, R., Rees, D. C., Kurtz, D. M., Scott, R. A., Huang, H., Adams, M. W. W. & Eidsness, M. K. (1998). *J. Biol. Inorg. Chem.* **3**, 484–493.

Berman, H. M., Westbrook, J., Feng, Z., Gilliland, G., Bhat, T. N., Weissig, H., Shindyalov, I. N. & Bourne, P. E. (2000). *Nucleic Acids Res.* **28**, 235–242.

Brünger, A. T. (1992). *Nature (London)*, **355**, 472–475.

Chatake, T., Kurihara, K., Tanaka, I., Tsyba, I., Bau, R., Jenney, F. E., Adams, M. W. W. & Nimura, N. (2004). *Acta Cryst.* D**60**, 1364–1373.

Chen, C.-J., Liu, M.-Y., Chen, Y.-T. & LeGall, J. (2003). *Biochem. Biophys. Res. Commun.* **308**, 684–688.

Cohen, G. N., Barbe, V., Flament, D., Galperin, M., Heilig, R., Lecomte, O., Poch, O., Prieur, D., Querellou, J., Ripp, R., Thierry, J.-C., Van der Oost, J., Weissenbach, J., Zivanovic, Y. & Forterre, P. (2003). *Mol. Microbiol.* **47**, 1495–1512.

Dauter, Z., Lamzin, V. S. & Wilson, K. S. (1997). *Curr. Opin. Struct. Biol.* **7**, 681–688.

Dauter, Z., Wilson, K. S., Sieker, L. C., Moulis, J. M. & Meyer, J. (1996). *Proc. Natl Acad. Sci. USA*, **93**, 8836–8840.

Day, M. W., Hsu, B. T., Joshua-Tor, L., Park, J.-B., Zhou, Z. H., Adams, M. W. W. & Rees, D. C. (1992). *Protein Sci.* **1**, 1494–1507.

Desiraju, G. R. & Steiner, T. (1999). *The Weak Hydrogen Bond.* Oxford University Press.

Eidsness, M. K., Burden, A. E., Richie, K. A., Kurtz, D. M. J., Scott, R. A., Smith, E. T., Ichiye, T., Beard, B., Min, T. & Kang, C. (1999). *Biochemistry*, **38**, 14803–14809.

Engh, R. A. & Huber, R. (2001). *International Tables for Crystallography*, Vol. F, edited by M. G. Rossmann & E. Arnold, pp. 382–392. Dordrecht: Kluwer.

Erauso, G., Reysenbach, A.-L., Godfroy, A., Meunier, J.-R., Crump, B., Partensky, F., Baross, J. A., Marteinsson, V., Barbier, G., Pace, N. R. & Prieur, D. (1993). *Arch. Microbiol.* **160**, 338–349.

Esposito, L., Vitagliano, L. & Mazzarella, L. (2002). *Protein Pept. Lett.* **9**, 95–105.

research papers

Esposito, L., Vitagliano, L., Sica, F., Sorrentino, G., Zagari, A. & Mazzarella, L. (2000). *J. Mol. Biol.* **297**, 713–732.

Esposito, L., Vitagliano, L., Zagari, A. & Mazzarella, L. (2000*a*). *Protein Sci.* **9**, 2038–2042.

Esposito, L., Vitagliano, L., Zagari, A. & Mazzarella, L. (2000*b*). *Protein Eng.* **13**, 825–828.

Fabiola, G. F. (1997). *Acta Cryst.* D**53**, 316–320.

Frey, M., Sieker, L., Payan, F., Haser, R., Bruschi, M., Pepe, G. & LeGall, J. (1987). *J. Mol. Biol.* **197**, 525–41.

Fuhrmann, C. N., Kelch, B. A., Ota, N. & Agard, D. A. (2004). *J. Mol. Biol.* **338**, 999–1013.

Guillot, B., Viry, L., Guillot, R., Lecomte, C. & Jelsch, C. (2001). *J. Appl. Cryst.* **34**, 214–223.

Howard, E. I., Sanishvili, R., Cachau, R. E., Mitschler, A., Chevrier, B., Barth, P., Lamour, V., Van Zandt, M., Sibley, E., Bon, C., Moras, D., Schneider, T. R., Joachimiak, A. & Podjarny, A. (2004). *Proteins*, **55**, 792–804.

Iwata, S., Saynovits, M., Link, T. A. & Michel, H. (1996). *Structure*, **4**, 567–579.

Jamal, S., Boraston, A. B., Turkenburg, J. P., Tarbouriech, N., Ducros, V. M.-A. & Davies, G. J. (2004). *Structure*, **12**, 1177–1187.

Jelsch, C., Teeter, M. M., Lamzin, V., Pichon-Pesme, V., Blessing, R. H. & Lecomte, C. (2000). *Proc. Natl Acad. Sci. USA*, **97**, 3171–3176.

Jenney, F. E., Verhagen, M. F. J. M., Cui, X. & Adams, M. W. W. (1999). *Science*, **286**, 306–309.

Jones, T. A., Cowan, S., Zou, J.-Y. & Kjeldgaard, M. (1991). *Acta Cryst.* A**47**, 110–119.

Kang, B. S., Devedjiev, Y., Derewenda, U. & Derewenda, Z. S. (2004). *J. Mol. Biol.* **338**, 483–493.

Karplus, P. A. (1996). *Protein Sci.* **5**, 1406–1420.

Ko, T.-P., Robinson, H., Gao, Y.-G., Cheng, C.-H. C., CeVries, A. L. & Wang, A. H.-J. (2003). *Biophys. J.* **84**, 1228–1237.

Kuemmerle, R., Zhuang-Jackson, H., Gaillard, J. & Moulis, J.-M. (1997). *Biochemistry*, **36**, 15983–15991.

Kuhn, P., Knapp, M., Soltis, S. M., Ganshaw, G., Thoene, M. & Bott, R. (1998). *Biochemistry*, **37**, 13446–13452.

Kurihara, K., Tanaka, I., Chatake, T., Adams, M. W. W., Jenney, F. E., Moiseeva, N., Bau, R. & Nimura, N. (2004). *Proc. Natl Acad. Sci. USA*, **101**, 11215–11220.

Lamzin, V. & Wilson, K. S. (1997). *Methods Enzymol.* **277**, 269–305.

Laskowski, R., MacArthur, M. W., Moss, D. S. & Thornton, J. M. (1993). *J. Appl. Cryst.* **26**, 283–291.

Lin, I. J., Gebel, E. B., Machonkin, T. E., Westler, W. M. & Markley, J. L. (2003). *J. Am. Chem. Soc.* **125**, 1464–1465.

Liu, L., Nogi, T., Kobayashi, M., Nozawa, T. & Miki, K. (2002). *Acta Cryst.* D**58**, 1085–1091.

Longenecker, K. L., Garrard, S. M., Sheffield, P. J. & Derewenda, Z. S. (2001). *Acta Cryst.* D**57**, 679–688.

MacArthur, M. W. & Thornton, J. M. (1996). *J. Mol. Biol.* **264**, 1180–1195.

Mateja, A., Devedjiev, Y., Krowarsh, D., Longenecker, K. L., Dauter, Z., Otlewski, J. & Derewenda, Z. S. (2002). *Acta Cryst.* D**58**, 1983–1991.

Merritt, E. A. (1999). *Acta Cryst.* D**55**, 1109–1117.

Min, T., Ergenekan, C. E., Eidsness, M. K., Ichiye, T. & Kang, C. (2001). *Protein Sci.* **10**, 613–621.

Mukherjee, M. (1999). *Acta Cryst.* D**55**, 820–825.

Murshudov, G. N., Vagin, A. A. & Dodson, E. J. (1997). *Acta Cryst.* D**53**, 240–255.

Navaza, J. (1994). *Acta Cryst.* A**50**, 157–163.

Otwinowski, Z. & Minor, W. (1997). *Methods Enzymol.* **276**, 307–326.

Park, I. Y., Eidsness, M. K., Lin, I.-J., Gebel, E. B., Youn, B., Harley, J. L., Machonkin, T. E., Frederick, R. O., Markley, J. L., Smith, E. T., Ichiye, T. & Kang, C. (2004). *Proteins*, **57**, 618–625.

Park, I. Y., Youn, B., Harley, J. L., Eidsness, M. K., Smith, E., Ichiye, T. & Kang, C. (2004). *J. Biol. Inorg. Chem.* **9**, 423–428.

Sheldrick, G. M. (1990). *Acta Cryst.* A**46**, 467–473.

Sheldrick, G. M. (1998). *Direct Methods for Solving Macromolecular Structures*, edited by S. Fortier, pp. 401–411. Dordrecht: Kluwer Academic Publishers.

Sheldrick, G. M., Dauter, Z., Wilson, K. S., Hope, H. & Sieker, L. C. (1993). *Acta Cryst.* D**49**, 18–23.

Sheldrick, G. M. & Schneider, T. R. (1997). *Methods Enzymol.* **276**, 307–326.

Schmidt, A., Jelsch, C., Ostergaard, P., Rypniewski, W. & Lamzin, V. S. (2003). *J. Biol. Chem.* **278**, 43357–43362.

Schmidt, A. & Lamzin, V. S. (2002). *Curr. Opin. Struct. Biol.* **12**, 698–703.

Schmidt, C. L., Hatzfeld, O. M., Petersen, A., Link, T. A. & Schäfer, G. (1997). *Biochem. Biophys. Res. Commun.* **234**, 283–287.

Swartz, P. D., Beck, B. W. & Ichiye, T. (1996). *Biophys. J.* **71**, 2958–2969.

Tronrud, D. E. (1997). *Methods Enzymol.* **277**, 243–268.

Wegner, P., Bever, M., Schünemann, V., Trautwein, A. X., Schmidt, C., Bönisch, H., Gnida, M. & Meyer-Klaucke, W. (2004). *Hyperfine Interact.* **156/157**, 293–298.

Zeng, Q., Smith, E. T., Kurtz, D. M. & Scott, R. A. (1996). *Inorg. Chim. Acta*, **242**, 245–251.